

Search for gravitational-wave signals associated with gamma-ray bursts during the second observing run of Advanced LIGO and Advanced Virgo

THE LIGO SCIENTIFIC COLLABORATION
THE VIRGO COLLABORATION
FRANCESCO CAROTENUTO^{1,2} AND BADRI KRISHNAN^{3,4}

¹*INFN, Sezione di Roma, I-00185 Roma, Italy*

²*Università di Roma “La Sapienza,” I-00185 Roma, Italy*

³*Max-Planck-Institut für Gravitationsphysik (Albert-Einstein-Institut), D-30167 Hannover, Germany*

⁴*Leibniz Universität Hannover, D-30167 Hannover, Germany*

(Dated: June 6, 2022)

ABSTRACT

We present the results of targeted searches for gravitational wave transients associated with gamma-ray bursts during the second observing run of Advanced LIGO and Advanced Virgo, which took place from November 2016 to August 2017. We have analyzed 98 gamma-ray bursts using an unmodeled search method that searches for generic transient gravitational waves and 42 with a modeled search method that targets compact-binary mergers as progenitors of short gamma-ray bursts. Both methods clearly detect the previously reported binary merger signal GW170817, with p -values of $<9.38 \times 10^{-6}$ (modeled) and 3.1×10^{-4} (unmodeled). We find no evidence of associated gravitational-wave signals for any of the other gamma-ray bursts analyzed, and therefore report lower bounds on the distance to each of these, assuming various source types and signal morphologies. Using our final modeled search results, short gamma-ray burst observations, and assuming binary neutron star progenitors, we place bounds on the rate of short gamma-ray bursts as a function of redshift for $z \leq 1$ and estimate 0.07–1.80 detections per year for the 2019-20 LIGO-Virgo observing run and 0.15–3.90 joint detections per year when current gravitational-wave detectors are operating at design sensitivities.

1. INTRODUCTION

Gamma-ray bursts (GRBs) are high energy astrophysical transients originating throughout the universe that are observed more than once per day on average. The prompt gamma ray emission is thought to emanate from highly relativistic jets powered by matter interacting with a compact central object such as an accreting black hole (BH) or a magnetar (Woosley 1993). Broadly speaking, GRBs are divided into two sub-populations based upon duration and spectral hardness (Kouveliotou et al. 1993).

Long-soft bursts generally have durations $\gtrsim 2$ seconds. The favored model is the core-collapse supernova (SN) of a rapidly rotating massive star (Woosley & Bloom 2006; Mösta et al. 2015). This connection was observationally supported by the presence of SN 1998bw within the error box of the long GRB 980425 (Galama et al. 1998) and the later strong association of SN 2003dh with GRB 030329 (Hjorth et al. 2003; Stanek et al. 2003). The core collapse process will produce some gravitational radiation (Fryer & New 2011). Rotational instabilities may give rise to much more signif-

icant gravitational wave (GW) emission, however, and could be observable from beyond the Milky Way (Fryer et al. 2002; Davies et al. 2002; Kobayashi & Meszaros 2003; Shibata et al. 2003; Piro & Pfahl 2007; Corsi & Meszaros 2009; Romero et al. 2010; Gossan et al. 2016).

Neutron star (NS) binaries have long been proposed as the progenitors of short-hard GRBs (Blinnikov et al. 1984; Paczynski 1986; Eichler et al. 1989; Narayan et al. 1992). The detection of the GW transient GW170817, a NS binary merger (Abbott et al. 2017a,e, 2019), in coincidence with the short GRB 170817A (Goldstein et al. 2017; Savchenko et al. 2017) confirmed that such mergers can produce short GRBs. An optical detection of a counterpart (Coulter et al. 2017) was followed by panchromatic observations identifying kilonova and afterglow emission (see Abbott et al. 2017f, and references therein).

The unusually low flux of GRB 170817A and its light curve evolution suggested an off-axis GRB with a relativistic structured jet or cocoon that either propagated into the universe successfully or was choked (Rossi et al. 2002; Kasliwal et al. 2017; Hallinan et al. 2017; Got-

tlieb et al. 2018; Lamb & Kobayashi 2017; Troja et al. 2017; Lazzati et al. 2018; Zhang et al. 2018). Later, very long baseline interferometry observations indicated a successfully launched relativistic jet (Mooley et al. 2018; Ghirlanda et al. 2019). The center of this jet appears to have been directed at an angle of approximately 15° – 30° from the line of sight (Lazzati et al. 2018; Mooley et al. 2018). Analysis of the first ten years of Fermi Gamma-ray Burst Monitor (GBM) data suggests GRB 170817A may belong to a population of local, low-luminosity short GRBs with similar spectral features (von Kienlin et al. 2019). The multimessenger observations of this event have proven to be extremely rich, providing insights about the structure of neutron stars (Margalit & Metzger 2017; Radice et al. 2018; Abbott et al. 2018a; Most et al. 2018; De et al. 2018), the local cosmological expansion rate (Abbott et al. 2017b, 2019; Hotokezaka et al. 2018), and heavy element nucleosynthesis (Drout et al. 2017; Cowperthwaite et al. 2017; Chornock et al. 2017; Smartt et al. 2017; Kasen et al. 2017; Abbott et al. 2017d) to name a few.

In this paper we present targeted GW follow-up of GRBs – long and short – reported during the second observing run of Advanced LIGO and Advanced Virgo (O2). The observing run spanned 30 November 2016 to 25 August 2017, with Advanced Virgo commencing observations on 1 August 2017. As a measure of their sensitivities, the Advanced LIGO instruments had sky- and orientation-averaged BNS ranges between 65–100 Mpc throughout the run, while for Advanced Virgo this range was approximately 25 Mpc (Abbott et al. 2018b). In addition to GW170817, seven binary BH mergers were previously identified during O2, with a further three binary BHs observed during the first observing run (Abbott et al. 2018b).

We discuss the population of GRBs included in our analyses in Section 2, and summarize the methods used in Section 3. We then present the results of a modeled binary merger analysis targeting short-hard GRBs in Section 4 and an unmodeled analysis targeting all GRBs in Section 5, with discussion in Section 6 followed by concluding remarks in Section 7.

2. GRB SAMPLE

The GRB sample contains events disseminated by the Gamma-ray Coordinates Network (GCN)¹, with additional information gathered from the Swift BAT

catalog² (Lien et al. 2016), the online Swift GRB Archive³, Fermi GBM Burst Catalog⁴ (Gruber et al. 2014; von Kienlin et al. 2014; Bhat et al. 2016), and the InterPlanetary Network (IPN) (Hurley et al. 2003)⁵. An automated system called VALID (Coyne 2015) cross-checks the time and localization parameters of the Swift and Fermi events against the published catalog with automated literature searches. In total, from November 2016 through August 2017, there were 242 bursts detected in the combined Swift + Fermi catalog. We received a total of 52 bursts localized by the IPN with many bursts appearing in both catalogs. GRBs that were poorly localized were removed from our sample, as were GRBs that did not occur during a period of stable, science-quality data taking by the available GW detectors.

For the purposes of this work, GRBs are classified (as in Abbott et al. 2017g) based on their T_{90} value – the period over which 90% of the flux was observed – and its uncertainty δT_{90} . GRBs with a value of $T_{90} + \delta T_{90} < 2$ s are *short*, and those with $T_{90} + \delta T_{90} > 4$ s are *long*. The remaining GRBs are *ambiguous*.

As in Abbott et al. (2017g), a generic unmodeled GW transient search (Sutton et al. 2010; Was et al. 2012) was performed for all GRBs for which 660 s of coincident data was available from two GW detectors, regardless of classification. A modeled search for coalescing binary GW signals (Harry & Fairhurst 2011; Williamson et al. 2014) was performed for all short and ambiguous GRBs with at least 1664 s of data in one or more detectors. This scheme resulted in 98 GRBs being analyzed with our unmodeled method and 42 analyzed with our modeled method.

3. SEARCH METHODS

To cover all possible gravitational-wave emission mechanisms we consider two search methods: a modeled search for binary merger signals from short or ambiguous GRBs, and an unmodeled search for GWs from all GRBs. Neither of these methods have changed since previous published results (Abbott et al. 2017g,a), so we provide summary overviews here.

3.1. Modeled search for binary mergers

² Swift BAT Gamma-Ray Burst Catalog: <http://swift.gsfc.nasa.gov/results/batgrbcatalog/>.

³ Swift GRB Archive: <http://swift.gsfc.nasa.gov/archive/grb-table/>.

⁴ FERMIGBRST - Fermi GBM Burst Catalog: <https://heasarc.gsfc.nasa.gov/W3Browse/fermi/fermigbrst.html>.

⁵ Collected via private communication with Kevin Hurley

¹ GCN Circulars Archive: <http://gcn.gsfc.nasa.gov/gcn3-archive.html>.

The modeled search is a coherent matched filtering pipeline known as PyGRB (Harry & Fairhurst 2011; Williamson et al. 2014), and is contained within the PyCBC data analysis toolkit⁶ (Nitz et al. 2018). We analyze a 6 s *on-source* window comprising $[-5, +1)$ s around the arrival time of the GRB for a GW candidate event, and up to approximately 90 minutes of adjacent data to characterize the background.

We use a bank of GW template waveforms for filtering (Owen & Sathyaprakash 1999) that encompasses combinations of masses and spins consistent with BNS and NS-BH systems that may be electromagnetically bright, i.e., under conservative assumptions about the NS equation of state, the evolution of these systems towards merger could feasibly produce an accretion disc via disruption of the NS that might be sufficient to power a GRB (Pannarale & Ohme 2014). The templates are restricted to orbital inclinations of 0° or 180° . This decision is motivated by the expectation that short GRBs do not have jets with angular sizes, and therefore inclinations, much greater than 30° (e.g., Fong et al. 2015). The effect of a small inclination angle on the relative amplitudes of the two GW polarizations is minor enough that restricting the inclination of templates to 0° or 180° can simultaneously reduce computational cost and improve sensitivity to slightly inclined systems by lowering the search background (Williamson et al. 2014). The templates are generated with an aligned-spin model tuned to numerical simulations of binary BHs (Khan et al. 2016). This model was chosen since it was found to provide good levels of signal recovery with relatively low computational cost, and all available models featuring matter effects or generic spin orientations would significantly increase the average computational cost per individual waveform generation and require a substantial increase in the number of templates. Filtering is performed over frequencies of 30–1000 Hz.

The detection statistic is a re-weighted, coherent matched filter signal-to-noise ratio (SNR) (Harry & Fairhurst 2011; Williamson et al. 2014). Candidate significance is evaluated by comparing the most prominent trigger within the 6 s *on-source*, if there is one, with the most prominent in each of the numerous 6 s *off-source* trials to produce a p -value for the *on-source* candidate. Extended background characterization is achieved using *time slides*; additional *off-source* trials are generated by combining data from GW detectors after introducing time shifts longer than the light travel time across the network.

⁶ <https://pycbc.org/>

Search sensitivity is estimated by injecting simulated signals into *off-source* data in software. We choose three distinct astrophysical populations of simulated signals: BNS, NS-BH with spins aligned with the orbital angular momentum, and NS-BH with generically oriented spins. Signals are simulated as having originated at a range of distances. The 90% exclusion distance, D_{90} , is the distance within which 90% of a simulated population are recovered with a ranking statistic greater than the most significant trigger in the *on-source*.

In all instances NS masses are drawn from a normal distribution of mean $1.4 M_\odot$ and standard deviation $0.2 M_\odot$ (Kiziltan et al. 2013; Özel & Freire 2016), restricted to the range $[1, 3] M_\odot$ where the upper limit is conservatively chosen based on theoretical consideration (Kalogera & Baym 1996). NS spin magnitudes are limited to ≤ 0.4 based upon the fastest observed pulsar spin (Hessels et al. 2006).

BH masses are drawn from a normal distribution of mean $10 M_\odot$ and standard deviation $6 M_\odot$, restricted to the range $[3, 15] M_\odot$, with spin magnitudes restricted to ≤ 0.98 , motivated by X-ray binary observations (e.g., Özel et al. 2010; Kreidberg et al. 2012; Miller & Miller 2014).

All simulations have binary orbital inclinations restricted to within $[0^\circ, 30^\circ]$ or $[150^\circ, 180^\circ]$. Additionally, the EM-bright condition is applied to simulations, avoiding the inclusion of systems that could not feasibly power a GRB (Pannarale & Ohme 2014).

For each of our three astrophysical populations we generate simulations with three different waveform models so as to account for modeling uncertainty. Specifically, the results quoted in this paper are obtained for simulations with a point-particle effective one body model tuned to numerical simulations, which incorporates orbital precession effects due to unaligned spins (Pan et al. 2014; Taracchini et al. 2014; Babak et al. 2017).

3.2. Unmodeled search for generic transients

We run an unmodeled search targeting all GRBs; long, short, and ambiguous. This analysis is implemented within the X-Pipeline software package (Sutton et al. 2010; Was et al. 2012). This is an unmodeled search since we do not know the specific signal shape of GW emission from the core collapse of massive stars, so we make minimal assumptions about the signal morphology. We use the time interval around a GRB trigger beginning 600 s before and ending either 60 s after or at the T_{90} time (whichever is larger) as the *on-source* window. This window is long enough to cover the time delay between GW emission from a progenitor and the

GRB (Koshut et al. 1995; Aloy et al. 2000; MacFadyen et al. 2001; Zhang et al. 2003; Lazzati 2005; Wang & Meszaros 2007; Burlon et al. 2008, 2009; Lazzati et al. 2009; Vedrenne & Atteia 2009). We restrict the search to the most sensitive frequency band of the GW detectors of 20–500 Hz. At lower frequencies terrestrial noise dominates and at higher frequencies ($f \gtrsim 300$) the GW energy necessary to produce a detectable signal scales as $\propto f^4$ Hz (see, e.g., section 2 of Abbott et al. 2017c).

Before analyzing detector data, we excise periods of poor quality data from the data stream. These periods include non-Gaussian noise transients, or *glitches*, that can be traced to environmental or instrumental causes (Nuttall 2018; Berger 2018). Including a detector data stream with low sensitivity and many glitches can reduce overall search sensitivity. Particular care was taken to ensure periods of poor quality data from the Virgo detector, which was significantly less sensitive than both LIGO detectors during O2, did not degrade the unmodeled search performance. For GRBs for which we have data from three interferometers, methods for flagging and removing poor quality data were tuned on off-source Virgo data, however ultimately Virgo data were only included in the final analysis if the sensitivity of the search was improved by its inclusion.

The analysis pipeline generates time-frequency maps of the GW data stream after coherently combining data from all detectors. These maps are scanned for clusters of pixels with excess energy, referred to as *events*, which are ranked according to a detection statistic based on energy. Coherent consistency tests are applied to reject events associated with noise transients based on correlations between data in different detectors. The surviving event with the largest ranking statistic is taken to be the best candidate for a GW detection and we evaluate its significance in the same way as the modeled analysis except with 660s long off-source trials.

As in the modeled search, we estimate the sensitivity of the unmodeled search by injecting simulated signals into off-source data in software. Here, we report results using signals from a stellar collapse model represented by circular sine-Gaussian (CSG) waveforms (see Equation 1 and Section 3.2 of Abbott et al. 2017g), with an optimistic total radiated energy $E_{\text{GW}} = 10^{-2} M_{\odot} c^2$ and fixed Q factor of 9. We construct four sets of such waveforms with central frequencies of 70, 100, 150, and 300 Hz. For an optimistic example of longer duration GW emission detectable by the unmodeled search we also report results for five accretion disk instability (ADI) waveforms (van Putten 2001; van Putten et al. 2014). In ADI models, GWs are emitted when instabilities form in a magnetically suspended torus around a rapidly spin-

ning BH. The model specifics and parameters used to generate these ADI models are the same as in Table 1 and Section 3.2 of Abbott et al. (2017g).

4. MODELED SEARCH RESULTS

We analyzed 42 short and ambiguous GRBs with the modeled search during O2. As previously reported, the analysis identifies GW170817 in association with GRB 170817A (Abbott et al. 2017e) in a manner consistent with other GW analyses (Abbott et al. 2017a, 2019). In our analysis of GRB 170817A reported here, where improved data calibration and noise subtraction has been incorporated, this signal was seen with a measured p -value of $< 9.38 \times 10^{-6}$ and a coherent SNR of 31.26, far in excess of the loudest background.

We found no other GW signals detected in association with any of the other GRBs. The p -value distribution for the 41 GRBs other than GRB 170817A is shown in Figure 1. For GRBs without any associated on-source trigger we plot an upper limit on the p -value of one, and a lower limit given by counting the background trials that similarly had no trigger. The expected distribution under the no-signal hypothesis is shown by the dashed black line, with dotted lines denoting a 2σ deviation about the no-signal distribution. To quantify population consistency with the no-signal hypothesis we use the weighted binomial test outlined in Abadie et al. (2012b). This test considers the lowest 5% of p -values in the population, weighted by the prior probability of detection based on the detector network sensitivity at the time and in the direction of the GRB. We do not include GW170817 as it is a definite GW detection. This results in a p -value of 0.30, thus we find no significant evidence for a population of unidentified subthreshold signals.

In addition to GRB 170817A, there were 6 instances of on-source candidates with p -values less than 0.1. The second most significant p -value was 0.0068, associated with GRB 170125102 from the Fermi GBM burst catalog. These 6 candidates were the subjects of further data quality checks to assess whether they could be caused by known instrumental noise sources. After careful scrutiny of the data there were no clear noise artifacts identified as being responsible for any of these candidates. We also ran Bayesian parameter estimation analyses using LALInference (Veitch et al. 2015) to quantify the evidence for a coherent subthreshold signal in the data versus incoherent or Gaussian instrumental noise. The results of these studies are summarized in more detail in Table 2. In particular, we quote Bayes factors (BFs) to quantify the support for a coherent signal over incoherent or Gaussian noise, where a value less than one favors noise over signal, and values greater than ~ 3 are

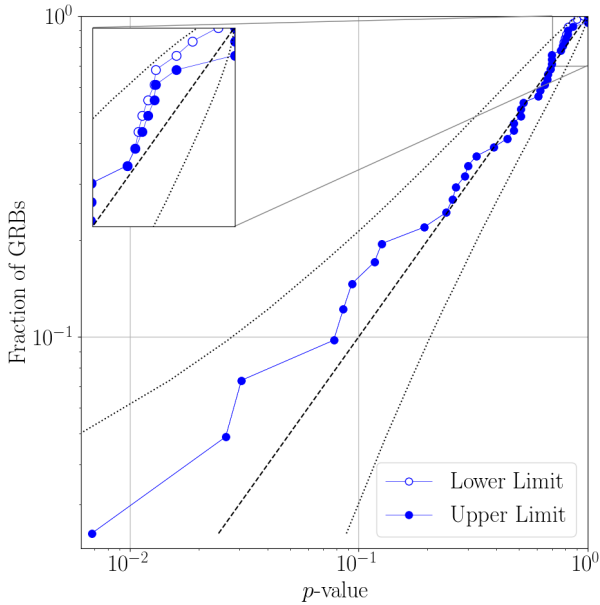


Figure 1. The cumulative distribution of event p -values for the NS binary search in O2. If the search reports no trigger in the on-source we plot an upper limit on the p -value of 1, and a lower limit equal to the number of off-source trials that contained no trigger. The dashed line indicates the expected distribution of p -values under the no-signal hypothesis, with the corresponding 2σ envelope marked by dotted lines.

generally required before considering support to be substantial (Kass & Raftery 1995). Some studies have previously looked at the distributions of these BFIs in the presence of weak signals and instrumental noise (Veitch & Vecchio 2008; Isi et al. 2018), albeit in somewhat different contexts to the low-mass targeted coherent search reported here. An in-depth study tailored to this analysis is beyond the scope of this work. However, our follow-up results are consistent with that of the modeled search itself, namely that there is no significant evidence for the presence of signals in addition to GW170817.

GRB 170817A is known to have originated at a distance of ~ 43 Mpc in the galaxy NGC 4993 (Abbott et al. 2017e). We have plotted the cumulative 90% exclusion distances for the remaining short and ambiguous GRBs in Figure 2. For each of our three simulated signal classes we quote the median of the 41 D_{90} results in Table 1.

5. UNMODELED SEARCH RESULTS

98 GRBs were analyzed using the generic transient method and no significant events were found except for GRB 170817A. The generic method recovered a signal for GRB 170817A consistent with the previously

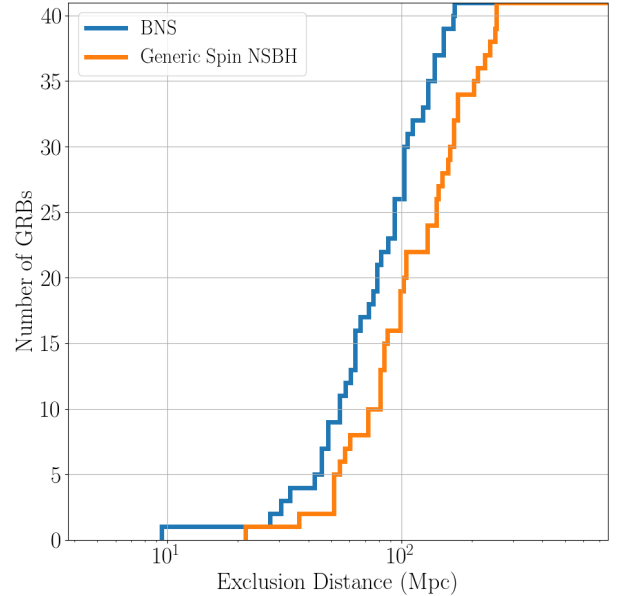


Figure 2. Cumulative histograms of the 90% confidence exclusion distances, D_{90} , for the BNS (blue) and generically spinning NS-BH (orange) signal models, shown for the sample of 41 short and ambiguous GRBs that did not have an identified GW counterpart. For a given GRB and signal model, D_{90} is the distance within which 90% of simulated signals inserted into off-source data are recovered with greater significance than the most significant on-source trigger.

reported signal GW170817 at a p -value of 3.1×10^{-4} . This value differs slightly from that reported in Abbott et al. (2017e), which can be explained by various changes in the configuration of X-Pipeline. Firstly, the clustering of pixels in time-frequency maps was previously done over a 7×7 pixel grid, whereas in the analysis reported here all clustering is done in a 3×3 grid. Secondly, in the case of GRB 170817A the coherent veto tests were tuned (as described in section III of (Sutton et al. 2010)) to maximize the sensitivity of the search to injections of BNS waveforms on the 99.99999th percentile loudest data segment. Here, we go back to the coherent veto tuning used in previous searches which uses the background data segment containing the 95th percentile loudest background event to all injected waveform families.

For the population of results we have compared the distribution of p -values against the expected distribution under the no-signal hypothesis. We find a combined p -value of 0.75 (0.75 in O1) looking at the most significant 5% of events from the unmodeled search using the weighted binomial test from Abadie et al. (2012a).

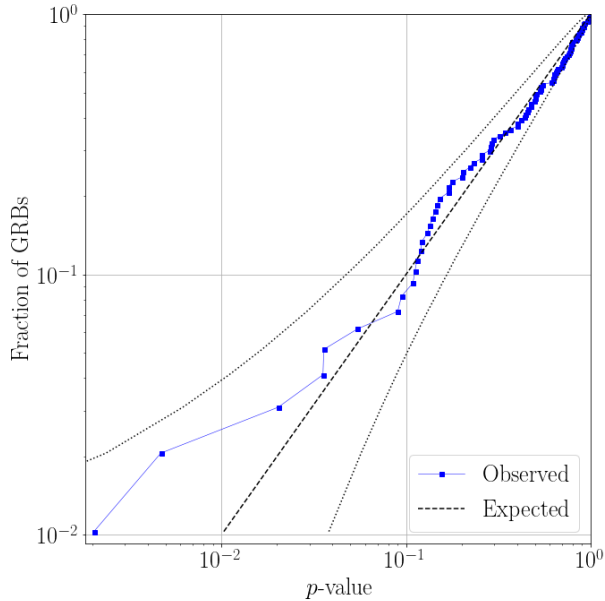


Figure 3. Cumulative distribution of p -values from the unmodeled search for transient GWs associated with 97 GRBs. The dashed line represents the expected distribution under the no-signal hypothesis, with dotted lines indicating a 2σ deviation from this distribution. These results are consistent with the no-signal hypothesis, and have a combined p -value of 0.75 as calculated by a weighted binomial test (Abadie et al. 2012a).

For GRBs other than GRB 170817A we place 90% confidence level lower limits on the distance D_{90} assuming various emission models. The limit depends on detector sensitivity that changes over time and sky location, systematic errors due to mismatch of a true GW signal and the waveforms used in simulations, as well as amplitude and phase errors from detector calibration. For all GRBs searched with the generic transient method we place exclusion limits that vary from 15 Mpc to 113 Mpc, depending on the GW signal model (Table 2). Some of these limits differ by an order of magnitude due to our limited knowledge of burst-type source emission models. The median D_{90} values compare favorably with those from the first observing run, either increasing or staying the same depending on the specific signal model.

6. DISCUSSION

Aside from GW170817, no GWs associated with GRBs were detected in O2. The median D_{90} values for each class of signal/source type provides an estimate of roughly how sensitive the searches were to such signals over the course of the entirety of O2, and these are given in Table 1. In Table 3 we provide information

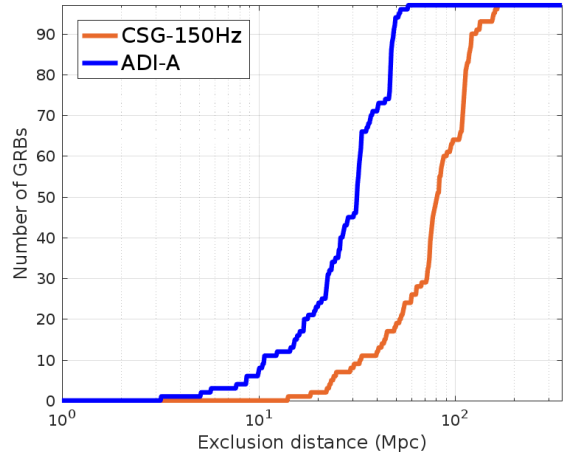


Figure 4. Cumulative histograms of the 90% confidence exclusion distances D_{90} for accretion disk instability signal model A (van Putten 2001; van Putten et al. 2014) and circular sine-Gaussian 150 Hz (Abbott et al. 2017g) model. For a given GRB and signal model this is the distance within which 90% of simulated signals inserted into off-source data are successfully recovered with a significance greater than the loudest on-source trigger. The median values for ADI-A and CSG-150 waveforms are 32 Mpc and 81 Mpc respectively.

on each GRB that was analyzed, including selected D_{90} results where relevant.

The non-detection of GW counterparts for 41 short and ambiguous GRBs analyzed by PyGRB can be combined with observed GRBs and the observation of GW170817 to obtain bounds on the short GRB-BNS rate as a function of redshift.

To evaluate this rate given the uncertainty in the jet structure profile of the short GRB population, we model the GRB luminosity function as a broken power law following Wanderman & Piran (2015), but extended at low luminosities with a second break with an associated free parameter γ_L , as in Abbott et al. (2017e). This extension at low luminosity is an effective model of the short GRB jet structure that yields low luminosities for mergers seen at a wide angle from their rotation axis.

$$\phi_o(L_i) = \begin{cases} \left(\frac{L_i}{L_{**}}\right)^{-\gamma_L} \left(\frac{L_{**}}{L_*}\right)^{-\alpha_L} & L_i < L_{**} \\ \left(\frac{L_i}{L_*}\right)^{-\alpha_L} & L_{**} < L_i < L_* \\ \left(\frac{L_i}{L_*}\right)^{-\beta_L} & L_i > L_* \end{cases}, \quad (1)$$

where L_i is the isotropic equivalent energy, and the parameters $L_* \simeq 2 \times 10^{52} \text{ergs}^{-1}$, $L_{**} \simeq 5 \times 10^{49} \text{ergs}^{-1}$, $\alpha_L \simeq 1$ and $\beta_L \simeq 2$ were used to fit the observed short GRBs redshift distribution. We assume

a threshold value for detectability in Fermi-GBM of 2 photons $\text{cm}^{-2}\text{s}^{-1}$ for the 64ms peak photon flux in the 50-300 keV band. Furthermore, we model the short GRB spectrum using a Band function with $E_{\text{peak}} = 800 \text{ keV}$, $\alpha_{\text{Band}} = -0.5$ and $\beta_{\text{Band}} = -2.25$. This yields an observed redshift distribution normalized by a total Fermi-GBM detection rate of 40 short GRBs per year.

In order to constrain the free parameter γ_L we start with an uninformative prior on γ_L , which yields a flat prior on the logarithm of the local rate density. Using the redshift distribution for a given γ_L we use Monte Carlo sampling to compute the probability of obtaining the O2 results presented here (41 non-detections and a single detection). This yields a posterior on γ_L with 90% confidence bounds of [0.04, 0.98]. The corresponding rates as a function of redshift are shown in Figure 5 in magenta.

These bounds can be compared to other measurements and models of the short GRB redshift distribution. For instance, the sample of observed short GRB redshifts without GRB 170817A is shown in Figure 5 by the brown lines (Abbott et al. 2017e, and references therein). We also show the cumulative Fermi detection rate as a function of redshift in green, calculated following the framework in Howell et al. (2018). This assumes that all short GRBs are associated with BNS mergers and estimates the Fermi-GBM detection rate by scaling the BNS source rate evolution with redshift by the Fermi-GBM detection efficiency. Finally, the current estimate of the local BNS merger rate of $1210^{+3230}_{-1040} \text{ Gpc}^{-3} \text{ yr}^{-1}$ (Abbott et al. 2018b) is shown in black for reference. We find that the posterior bounds from the modeled O2 GRB analysis overlap with the BNS merger rate and Fermi-GBM detected short GRB rate at low redshift. At high redshift there is agreement with the observed short GRB redshift distribution and the Fermi-GBM detection rate.

For the 2019-2020 LIGO-Virgo observing run we expect to see 1–30 BNS coalescences, while at design sensitivity LIGO-Virgo could detect 4–97 BNS mergers per year. Using the framework provided in Howell et al. (2018) we find that joint GW-GRB detection rates are lower, estimated at 0.07–1.80 detections per year for the 2019-20 LIGO-Virgo observing run and 0.15–3.90 joint detections per year at design sensitivity.

7. CONCLUSIONS

We have performed targeted analyses for GWs in association with GRBs during O2, searching for NS binary merger signals from short GRBs with a modeled analysis and GW burst signals from all GRBs with an unmod-

Table 1. Median 90% confidence level exclusion distances, D_{90} , for the searches during O2. Modeled search results are shown for three classes of NS binary progenitor model, and unmodeled search results are shown for circular sine-Gaussian (CSG) (Abbott et al. 2017g) and accretion disk instability (ADI) (van Putten 2001; van Putten et al. 2014) models.

Modeled search	NS-BH		NS-BH	
(Short GRBs)	BNS	Generic Spins	Aligned Spins	
D_{90} [Mpc]	80	105	144	
Unmodeled search	CSG	CSG	CSG	CSG
(All GRBs)	70 Hz	100 Hz	150 Hz	300 Hz
D_{90} [Mpc]	112	113	81	38
Unmodeled search	ADI	ADI	ADI	ADI
(All GRBs)	A	B	C	D
D_{90} [Mpc]	32	104	40	15

eled analysis. GW170817 is confirmed by both methods as a strong detection associated with GRB 170817A, entirely consistent with previously published results. No further GW signals were found as a result of these analyses, and there is no strong evidence found in our results for subthreshold signals. We set lower bounds on the distances to progenitors for a number of emission models, which include the largest D_{90} values published so far for some individual GRBs (Abadie et al. 2012a; Abbott et al. 2017g).

Based on the results of the modeled search we performed a population model analysis in Section 6 and place bounds on a twice broken power law short GRB luminosity function that is consistent with both the measured BNS merger rate and the Fermi-GBM observed short GRB rate, and therefore with the hypothesis that BNS mergers are generally short GRB progenitors. Further multimessenger observations should provide tighter constraints on GRB emission models and event rates, and investigate whether NS-BH mergers also power short GRBs. We expect to observe 0.07–1.80 joint GRB-GW events per year in the 2019-2020 LIGO-Virgo observing run, and 0.15–3.90 per year at network design sensitivity.

The authors gratefully acknowledge the support of the United States National Science Foundation (NSF) for the construction and operation of the LIGO Laboratory and Advanced LIGO as well as the Science and Technology Facilities Council (STFC) of the United Kingdom, the Max-Planck-Society (MPS), and the State of

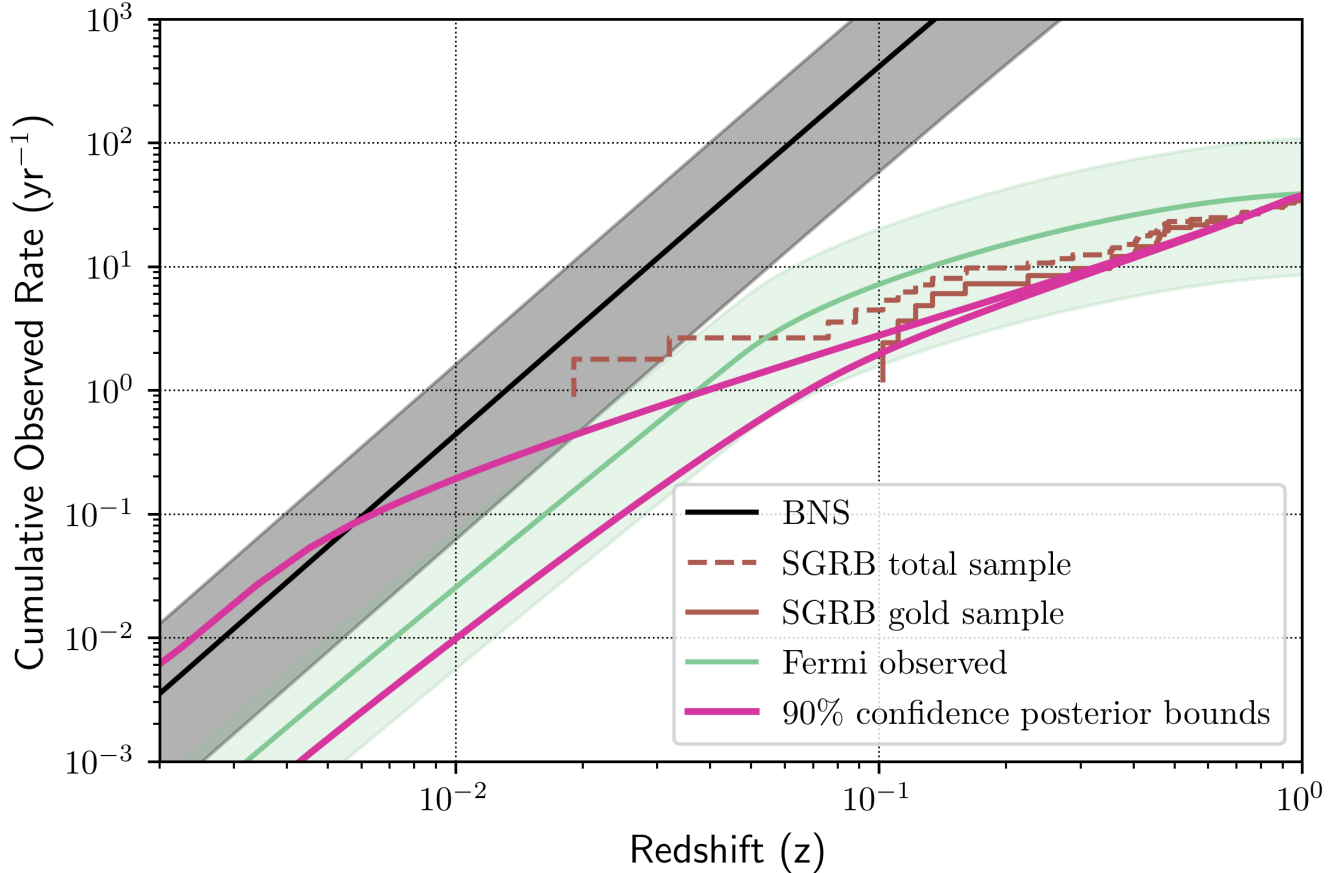


Figure 5. Predicted event rates per year as a function of redshift. The magenta lines show the 90% bounds on the rate associated with the fit of our model of the short GRB luminosity function (Eq. 1) to the O2 run results. In black we show the BNS merger rate $1210^{+3230}_{-1040} \text{ Gpc}^{-3} \text{ yr}^{-1}$ (Abbott et al. 2018b), and in green we show the Fermi-GBM short GRBs detection rate and its 90% credible interval (Howell et al. 2018). As a reference, the measured short GRBs redshift distribution without GRB 170817A is shown in brown (Abbott et al. 2017e, and references therein). Our analysis results shown in magenta are compatible with the BNS merger rate and the Fermi-GBM observed short GRB rate. This is consistent with the hypothesis that BNS mergers are generally short GRB progenitors.

Niedersachsen/Germany for support of the construction of Advanced LIGO and construction and operation of the GEO600 detector. Additional support for Advanced LIGO was provided by the Australian Research Council. The authors gratefully acknowledge the Italian Istituto Nazionale di Fisica Nucleare (INFN), the French Centre National de la Recherche Scientifique (CNRS) and the Foundation for Fundamental Research on Matter supported by the Netherlands Organisation for Scientific Research, for the construction and operation of the Virgo detector and the creation and support of the EGO consortium. The authors also gratefully acknowledge research support from these agencies as well as by the Council of Scientific and Industrial Research of India, the Department of Science and Technology, India, the Science & Engineering Research Board (SERB), India, the Ministry of Human Resource Development, India, the Spanish Agencia Estatal de Inves-

tigación, the Vicepresidència i Conselleria d’Innovació, Recerca i Turisme and the Conselleria d’Educació i Universitat del Govern de les Illes Balears, the Conselleria d’Educació, Investigació, Cultura i Esport de la Generalitat Valenciana, the National Science Centre of Poland, the Swiss National Science Foundation (SNSF), the Russian Foundation for Basic Research, the Russian Science Foundation, the European Commission, the European Regional Development Funds (ERDF), the Royal Society, the Scottish Funding Council, the Scottish Universities Physics Alliance, the Hungarian Scientific Research Fund (OTKA), the Lyon Institute of Origins (LIO), the Paris Île-de-France Region, the National Research, Development and Innovation Office Hungary (NKFIH), the National Research Foundation of Korea, Industry Canada and the Province of Ontario through the Ministry of Economic Development and Innovation, the Natural Science and Engineering Research Council

Canada, the Canadian Institute for Advanced Research, the Brazilian Ministry of Science, Technology, Innovations, and Communications, the International Center for Theoretical Physics South American Institute for Fundamental Research (ICTP-SAIFR), the Research Grants Council of Hong Kong, the National Natural Science

Foundation of China (NSFC), the Leverhulme Trust, the Research Corporation, the Ministry of Science and Technology (MOST), Taiwan and the Kavli Foundation. The authors gratefully acknowledge the support of the NSF, STFC, INFN and CNRS for provision of computational resources.

Table 2. Results of follow-up studies of PyGRB candidates with $p < 0.1$.

GRB Name	p -value	Comment
161210524	0.0933	BF = 1.45, giving only very weak evidence in favor of a coherent signal over noise. Chirp mass posterior is multimodal.
170125102	0.0068	BF = 0.88 not favoring coherent signal over noise. 1D posteriors show no significant information gain over priors.
170206453	0.0418	BF = 0.94 not favoring coherent signal over noise. Chirp mass posterior is multimodal.
170219002	0.0307	BF = 0.88 not favoring coherent signal over noise. 1D posteriors show minimal information gain over priors.
170614505	0.0856	BF = 0.46 not favoring coherent signal over noise. 1D posteriors show no significant information gain over priors.
170726249	0.0262	BF = 2.08, giving only very weak evidence in favor of a coherent signal over noise.

Table 3. Information and limits on associated GW emission for each of the analyzed GRBs. The Satellite column lists the instrument whose sky localization was used for the purposes of analysis. The Network column lists the GW detector network used in the analysis of each GRB – H1 = LIGO Hanford, L1 = LIGO Livingston, V1 = Virgo. A \dagger denotes cases in which the on-source window of the generic transient search is extended to cover the GRB duration ($T_{90} > 60$ s). In cases where each analysis used a different network, parentheses indicate the network used for PyGRB analysis, and detail is provided in the table footnotes. Columns 8–12 display the 90% confidence exclusion distances to the GRB (D_{90}) for several emission scenarios: BNS, generic and aligned spin NS-BH, ADI-A, and CSG GW burst at 150 Hz with total radiated energy $E_{\text{GW}} = 10^{-2} M_{\odot} c^2$.

GRB Name	UTC Time	R.A.	Dec.	Satellite(s)	Type	Network	BNS	Generic NS-BH	Aligned NS-BH	ADI-A	CSG 150 Hz	D_{90} (Mpc)	
												NS-BH	ADIA
161207224	05:22:47	19 ^h 39 ^m 14 ^s	-9°56′	Fermi	Long	H1L1	8	40
161207813	19:31:22	3 ^h 55 ^m 09 ^s	15°44′	Fermi	Long	H1L1	26	73
161210524	12:33:54	18 ^h 52 ^m 28 ^s	63°03′	Fermi	Ambiguous	H1L1	61	72	112	19	49
161212652	15:38:59	01 ^h 39 ^m 36 ^s	68°12′	Fermi	Ambiguous	H1	49	59	60
161217128	03:03:45	14 ^h 26 ^m 31 ^s	51°59′	Fermi	Ambiguous	H1L1	65	85	122	18	56
170111815	19:34:01	18 ^h 03 ^m 31 ^s	63°42′	Fermi	Ambiguous	H1	95	160	198
170111A	00:33:27	1 ^h 22 ^m 45 ^s	-32°33′	Swift	Long	H1L1	13	78
170112A	02:01:59	1 ^h 00 ^m 55 ^s	-17°14′	Swift	Short	H1L1	83	106	144	32	79
170113A	10:04:04	4 ^h 06 ^m 59 ^s	-71°56′	Swift	Long	H1L1	32	107
170121067	01:36:53	0 ^h 12 ^m 07 ^s	-75°37′	Fermi	Ambiguous	H1L1	79	105	144	26	73
170121133	03:10:52	16 ^h 07 ^m 57 ^s	13°49′	Fermi	Ambiguous	H1L1	96	142	172	23	88
170124238	05:42:12	19 ^h 26 ^m 57 ^s	69°37′	Fermi	Long	H1L1	25	72
170124528	12:40:29	00 ^h 43 ^m 24 ^s	11°01′	Fermi	Short	H1	65	101	116
170125022	00:31:14	17 ^h 36 ^m 34 ^s	28°34′	Fermi	Ambiguous	H1	46	52	57
170125102	02:27:10	23 ^h 57 ^m 38 ^s	-38°14′	Fermi	Short	H1L1(H1) ^a	30	39	63	20	51
170127067	01:35:47	22 ^h 37 ^m 19 ^s	-63°56′	Fermi	Short	H1L1	76	129	141	24	64
170127B	15:13:29	01 ^h 19 ^m 58 ^s	-30°20′	Swift	Short	H1	113	169	197
170130302	07:14:44	18 ^h 04 ^m 12 ^s	-29°07′	Fermi	Long	H1L1	48	121
170130510	12:13:48	20 ^h 35 ^m 00 ^s	1°26′	Fermi	Long	H1L1 [†]	26	68
170202A	18:28:02	10 ^h 10 ^m 06 ^s	5°01′	Swift	Long	H1L1	47	113
170203486	11:40:25	16 ^h 20 ^m 21 ^s	-0°31′	Fermi	Short	H1L1	66	99	119	10	81
170203A	00:03:41	22 ^h 11 ^m 26 ^s	25°11′	Swift	Long	H1L1	38	112
170206A	10:51:58	14 ^h 12 ^m 43 ^s	12°34′	IPN	Short	H1L1	151	254	264	50	122
170208553	13:16:33	18 ^h 57 ^m 40 ^s	-0°07′	Fermi	Long	H1L1	31	64
170208A	18:11:16	11 ^h 06 ^m 10 ^s	-46°47′	Swift	Long	H1L1	50	134
170208B	22:33:38	8 ^h 28 ^m 34 ^s	-9°02′	Swift	Long	H1L1 [†]	32	77
170210116	02:47:36	15 ^h 04 ^m 14 ^s	-65°06′	Fermi	Long	H1L1 [†]	49	122
170212034	00:49:00	10 ^h 20 ^m 24 ^s	-1°29′	Fermi	Long	H1L1	29	76
170219002	00:03:07	3 ^h 39 ^m 21 ^s	50°04′	Fermi	Short	H1L1	171	251	304	52	159
170219110	02:38:04	5 ^h 14 ^m 45 ^s	-41°14′	Fermi	Long	H1L1	10	33

Table 3 continued

Table 3 (continued)

GRB Name	UTC Time	R.A.	Dec.	Satellite(s)	Type	Network	BNS	Generic NS-BH	Aligned NS-BH	ADFA	CSG 150 Hz	D_{90} (Mpc)	
												ADFA	CSG 150 Hz
170222A	05:00:59	19 ^h 31 ^m 53 ^s	28°04′	IPN	Short	HLL1	80	86	112	23	60		
170302166	03:58:24	10 ^h 17 ^m 00 ^s	29°23′	Fermi	Ambiguous	HLL1	107	175	206	47	109		
170304003	00:04:26	22 ^h 02 ^m 00 ^s	-73°46′	Fermi	Short	HLL1	105	143	178	34	85		
170305256	06:09:06	2 ^h 34 ^m 38 ^s	12°05′	Fermi	Short	HLL1(L1) ^b	48	73	82	10	14		
170306130	03:07:17	10 ^h 31 ^m 31 ^s	27°45′	Fermi	Long	HLL1	45	111		
170310417	09:59:50	14 ^h 33 ^m 14 ^s	53°59′	Fermi	Long	HLL1	50	135		
170310883	21:11:43	10 ^h 26 ^m 43 ^s	41°34′	Fermi	Long	HLL1	5	23		
170311	13:45:09	23 ^h 43 ^m 48 ^s	33°24′	IPN	Long	HLL1	34	92		
170311A	08:08:42	18 ^h 42 ^m 09 ^s	-30°02′	Swift	Long	HLL1	22	43		
170317A	09:45:59	6 ^h 12 ^m 20 ^s	50°30′	Swift	Long	HLL1	33	80		
170318A	12:11:56	20 ^h 22 ^m 39 ^s	28°24′	Swift	Long	HLL1†	47	119		
170318B	15:27:52	18 ^h 57 ^m 10 ^s	6°19′	Swift	Short	HLL1	152	254	281	48	112		
170323058	01:23:23	9 ^h 40 ^m 45 ^s	-38°60′	Fermi	Long	HLL1	28	75		
170325331	07:56:58	8 ^h 29 ^m 55 ^s	20°32′	Fermi	Short	HLL1	73	88	125	33	77		
170330A	22:29:51	18 ^h 53 ^m 17 ^s	-13°27′	Swift	Long	HLL1†	41	110		
170331A	01:40:46	21 ^h 35 ^m 06 ^s	-24°24′	Swift	Long	HLL1	49	119		
170402285	06:50:54	22 ^h 01 ^m 26 ^s	-10°38′	Fermi	Long	HLL1	9	110		
170402961	23:03:25	20 ^h 31 ^m 40 ^s	-45°56′	Fermi	Long	HLL1	48	113		
170403583	13:59:18	17 ^h 48 ^m 19 ^s	14°31′	Fermi	Short	HLL1	166	240	261		
170403707	16:57:33	16 ^h 24 ^m 09 ^s	41°49′	Fermi	Long	HLL1	24	54		
170409112	02:42:00	23 ^h 10 ^m 19 ^s	-7°04′	Fermi	Long	HLL1†	20	106		
170414551	13:13:16	2 ^h 54 ^m 00 ^s	75°53′	Fermi	Long	HLL1	33	80		
170416583	14:00:05	18 ^h 56 ^m 52 ^s	-57°01′	Fermi	Long	HLL1†	9	24		
170419983	23:36:14	17 ^h 39 ^m 28 ^s	-11°14′	Fermi	Long	HLL1	49	119		
170419A	13:26:40	5 ^h 19 ^m 25 ^s	-21°26′	Swift	Long	HLL1	48	114		
170422343	08:13:54	12 ^h 34 ^m 31 ^s	16°49′	Fermi	Long	HLL1	47	114		
170423719	17:15:08	22 ^h 57 ^m 21 ^s	-4°16′	Fermi	Long	HLL1	36	98		
170423872	20:55:23	13 ^h 58 ^m 24 ^s	26°22′	Fermi	Long	HLL1	17	45		
170424	10:12:06	10 ^h 00 ^m 40 ^s	-13°41′	IPN	Long	HLL1	32	75		
170424425	10:12:30	22 ^h 54 ^m 07 ^s	-45°12′	Fermi	Long	HLL1	32	74		
170428136	03:16:17	0 ^h 19 ^m 02 ^s	56°14′	Fermi	Long	HLL1	23	75		
170428A	09:13:42	22 ^h 00 ^m 12 ^s	26°55′	Swift	Short	HLL1	105	167	178	32	86		
170430204	04:54:20	01 ^h 35 ^m 26 ^s	30°07′	Fermi	Short	H1	32	54	81		
170501467	11:11:53	6 ^h 28 ^m 02 ^s	13°43′	Fermi	Long	HLL1	34	84		
170506169	04:02:48	7 ^h 29 ^m 02 ^s	51°52′	Fermi	Ambiguous	HLL1	103	174	149	36	84		
170604603	14:28:05	22 ^h 41 ^m 36 ^s	40°42′	Fermi	Short	L1	131	204	237		
170610689	16:31:47	4 ^h 35 ^m 38 ^s	46°29′	Fermi	Long	HLL1	53	162		
170611937	22:29:35	11 ^h 34 ^m 19 ^s	-7°22′	Fermi	Long	HLL1	32	75		
170614255	06:06:41	4 ^h 42 ^m 12 ^s	37°56′	Fermi	Long	HLL1†	22	55		

Table 3 continued

Table 3 (continued)

D_{90} (Mpc)												
GRB Name	UTC Time	R.A.	Dec.	Satellite(s)	Type	Network	BNS	Generic NS-BH	Aligned NS-BH	ADFA	CSG 150 Hz	
170614505	12:06:39	20 ^h 43 ^m 58 ^s	-37°54′	Fermi	Ambiguous	H1	9	22	0	
170616165	03:58:07	3 ^h 18 ^m 02 ^s	19°40′	Fermi	Long	H1L1†	34	95	
170618475	11:24:41	0 ^h 59 ^m 19 ^s	26°44′	Fermi	Long	H1L1	48	130	
170625692	16:35:47	7 ^h 06 ^m 48 ^s	-69°21′	Fermi	Long	H1L1	33	84	
170626A	09:37:23	11 ^h 01 ^m 37 ^s	56°29′	Swift	Long	H1L1	33	82	
170629A	12:53:33	8 ^h 39 ^m 50 ^s	-46°35′	Swift	Long	H1L1	48	117	
170705200	04:48:30	23 ^h 58 ^m 02 ^s	-21°56′	Fermi	Long	H1L1	29	74	
170705244	05:50:45	15 ^h 50 ^m 26 ^s	-7°26′	Fermi	Long	H1L1	32	86	
170705A	02:45:47	12 ^h 46 ^m 50 ^s	18°18′	Swift	Long	H1L1†	47	156	
170708046	01:06:11	22 ^h 13 ^m 00 ^s	25°37′	Fermi	Short	L1	57	105	103	
170709334	08:00:24	20 ^h 40 ^m 10 ^s	02°12′	Fermi	Ambiguous	L1	139	228	255	
170714A	12:25:32	2 ^h 17 ^m 17 ^s	1°58′	Swift	Long	H1L1†	48	123	
170715878	21:04:13	19 ^h 08 ^m 52 ^s	-16°37′	Fermi	Long	H1L1	47	114	
170723076	01:49:10	9 ^h 03 ^m 45 ^s	-19°26′	Fermi	Long	H1L1	26	75	
170723677	16:15:27	1 ^h 28 ^m 16 ^s	62°41′	Fermi	Long	H1L1	37	111	
170723882	21:10:18	14 ^h 10 ^m 19 ^s	39°50′	Fermi	Ambiguous	H1L1	95	83	179	40	110	
170724A	00:48:44	10 ^h 00 ^m 14 ^s	-1°02′	Swift	Long	H1L1†	21	84	
170726249	05:58:15	11 ^h 05 ^m 40 ^s	-34°00′	Fermi	Ambiguous	H1L1	124	152	207	38	112	
170728A	06:53:28	3 ^h 55 ^m 36 ^s	12°10′	Swift	Short	H1L1	89	129	163	26	81	
170731751	18:01:39	16 ^h 20 ^m 48 ^s	64°18′	Fermi	Long	H1L1†	17	44	
170802638	15:18:24	3 ^h 29 ^m 12 ^s	-39°13′	Fermi	Ambiguous	H1L1V1	45	62	72	3	24	
170803172	04:07:15	5 ^h 06 ^m 00 ^s	23°60′	Fermi	Ambiguous	H1L1(H1L1V1) ^c	56	83	105	16	53	
170803B	22:00:32	00 ^h 56 ^m 53 ^s	06°34′	IPN	Short	L1 ^d	140	215	234	
170804A	12:01:37	0 ^h 25 ^m 37 ^s	-64°47′	Swift	Long	H1V1†	15	45	
170805901	21:37:49	16 ^h 15 ^m 52 ^s	36°23′	Fermi	Long	H1V1	11	25	
170805A	14:38:10	20 ^h 50 ^m 26 ^s	22°28′	IPN	Short	H1L1V1	69	100	114	22	61	
170805B	14:18:49	8 ^h 40 ^m 32 ^s	70°06′	IPN	Short	H1L1V1	132	163	218	33	114	
170807A	21:56:09	9 ^h 33 ^m 44 ^s	-17°21′	Swift	Long	H1L1	27	76	
170808065	01:34:09	0 ^h 13 ^m 12 ^s	62°18′	Fermi	Ambiguous	L1V1	58	83	87	11	18	
170808936	22:27:43	9 ^h 42 ^m 38 ^s	2°11′	Fermi	Long	L1V1	22	41	
170809	23:46:26	16 ^h 52 ^m 37 ^s	-12°18′	IPN	Long	H1L1V1	27	87	
170816258	06:11:11	0 ^h 42 ^m 48 ^s	-15°37′	Fermi	Long	H1L1†	17	55	
170816599	14:23:03	23 ^h 25 ^m 36 ^s	19°06′	Fermi	Short	H1L1V1(H1V1) ^c	46	56	73	15	34	
170817908	21:47:34	5 ^h 32 ^m 07 ^s	50°04′	Fermi	Ambiguous	H1V1	35	51	63	16	30	
170817A	12:41:06	13 ^h 09 ^m 36 ^s	-23°24′	Fermi	Ambiguous	H1L1V1	N/A	N/A	N/A	N/A	N/A	
170818137	03:17:20	19 ^h 48 ^m 53 ^s	06°21′	Fermi	Ambiguous	H1L1	103	146	169	
170821265	06:22:00	16 ^h 51 ^m 26 ^s	19°07′	Fermi	Long	H1L1†	33	76	
170822A	09:11:51	6 ^h 17 ^m 29 ^s	54°60′	Swift	Long	H1L1V1†	32	97	
170823A	22:16:48	12 ^h 34 ^m 51 ^s	35°33′	Swift	Long	H1L1†	58	166	

Table 3 continued

Table 3 (continued)

D_{90} (Mpc)											
GRB Name	UTC Time	R.A.	Dec.	Satellite(s)	Type	Network	BNS	Generic NS-BH	Aligned NS-BH	ADFA	CSG 150 Hz
170825307	07:22:01	18 ^h 17 ^m 36 ^s	-26°12'	Fermi	Long	L1V1	15	31
170825500	12:00:06	0 ^h 14 ^m 33 ^s	20°07'	Fermi	Long	HIL1	47	116
170825784	18:49:11	7 ^h 45 ^m 16 ^s	-48°43'	Fermi	Long	HIL1V1 [†]	6	22

^a GRB 170125102 occurred when the Livingston detector was not in its nominal observing state, however the data was deemed suitable for the purposes of the unmodeled analysis.

^b GRB 170305256 occurred near the null of the Hanford detector and inclusion of its data degraded the PyGRB search sensitivity compared to a Livingston-only analysis.

^c GRB 170803172: Virgo data did not meet the data quality requirements of **X-Pipeline**.

^d GRB 170803B occurred near the null of the Virgo detector (see note *b*). In addition, Livingston data did not meet the data quality requirements of **X-Pipeline**, so this GRB was not subject to the unmodeled analysis.

^e GRB 170816599 occurred near the null of the Livingston detector (see note *b*).

REFERENCES

- Abadie, J., et al. 2012a, *Astrophys. J.*, 760, 12
— 2012b, *Phys. Rev.*, D85, 082002
- Abbott, B., et al. 2017a, *Phys. Rev. Lett.*, 119, 161101
- Abbott, B. P., et al. 2017b, *Nature*, 551, 85
— 2017c, *Phys. Rev.*, D95, 042003
— 2017d, *Astrophys. J.*, 850, L39
— 2017e, *Astrophys. J.*, 848, L13
— 2017f, *Astrophys. J.*, 848, L12
— 2017g, *Astrophys. J.*, 841, 89
— 2018a, *Phys. Rev. Lett.*, 121, 161101
— 2018b, arXiv:1811.12907
— 2019, *Phys. Rev.*, X9, 011001
- Aloy, M. A., Mueller, E., Ibanez, J. M., Marti, J. M., & MacFadyen, A. 2000, *Astrophys. J.*, 531, L119
- Babak, S., Taracchini, A., & Buonanno, A. 2017, *Phys. Rev.*, D95, 024010
- Berger, B. K. 2018, *Journal of Physics: Conference Series*, 957, 012004
- Bhat, P. N., et al. 2016, *Astrophys. J. Suppl.*, 223, 28
- Blinnikov, S. I., Novikov, I. D., Perevodchikova, T. V., & Polnarev, A. G. 1984, *Soviet Astronomy Letters*, 10, 177
- Burlon, D., Ghirlanda, G., Ghisellini, G., Greiner, J., & Celotti, A. 2009, *Astron. Astrophys.*, 505, 569
- Burlon, D., Ghirlanda, G., Ghisellini, G., et al. 2008, *Astrophys. J.*, 685, L19
- Chornock, R., et al. 2017, *Astrophys. J.*, 848, L19
- Corsi, A., & Meszaros, P. 2009, *Astrophys. J.*, 702, 1171
- Coulter, D. A., et al. 2017, *Science*, arXiv:1710.05452, [Science358,1556(2017)]
- Cowperthwaite, P. S., et al. 2017, *Astrophys. J.*, 848, L17
- Coyne, R. 2015, PhD thesis, The George Washington University
- Davies, M. B., King, A., Rosswog, S., & Wynn, G. 2002, *Astrophys. J.*, 579, L63
- De, S., Finstad, D., Lattimer, J. M., et al. 2018, *Phys. Rev. Lett.*, 121, 091102, [Erratum: *Phys. Rev. Lett.*121,no.25,259902(2018)]
- Drout, M. R., et al. 2017, *Science*, 358, 1570
- Eichler, D., Livio, M., Piran, T., & Schramm, D. N. 1989, *Nature*, 340, 126, [682(1989)]
- Fong, W.-f., Berger, E., Margutti, R., & Zauderer, B. A. 2015, *Astrophys. J.*, 815, 102
- Fryer, C. L., Holz, D. E., & Hughes, S. A. 2002, *Astrophys. J.*, 565, 430
- Fryer, C. L., & New, K. C. B. 2011, *Living Rev. Rel.*, 14, 1
- Galama, T. J., et al. 1998, *Nature*, 395, 670
- Ghirlanda, G., Salafia, O. S., Paragi, Z., et al. 2019, *Science*, arXiv:1808.00469
- Goldstein, A., et al. 2017, *Astrophys. J.*, 848, L14
- Gossan, S. E., Sutton, P., Stuver, A., et al. 2016, *Phys. Rev.*, D93, 042002
- Gottlieb, O., Nakar, E., Piran, T., & Hotokezaka, K. 2018, *Mon. Not. Roy. Astron. Soc.*, 479, 588
- Gruber, D., et al. 2014, *Astrophys. J. Suppl.*, 211, 12
- Hallinan, G., et al. 2017, *Science*, 358, 1579
- Harry, I. W., & Fairhurst, S. 2011, *Phys. Rev.*, D83, 084002
- Hessels, J. W. T., Ransom, S. M., Stairs, I. H., et al. 2006, *Science*, 311, 1901
- Hjorth, J., et al. 2003, *Nature*, 423, 847
- Hotokezaka, K., Nakar, E., Gottlieb, O., et al. 2018, arXiv:1806.10596
- Howell, E. J., Ackley, K., Rowlinson, A., & Coward, D. 2018, arXiv:1811.09168
- Hurley, K., Cline, T., Mitrofanov, I., et al. 2003, *AIP Conf. Proc.*, 662, 473
- Isi, M., Smith, R., Vitale, S., et al. 2018, *Phys. Rev.*, D98, 042007
- Kalogera, V., & Baym, G. 1996, *Astrophys. J.*, 470, L61
- Kasen, D., Metzger, B., Barnes, J., Quataert, E., & Ramirez-Ruiz, E. 2017, *Nature*, arXiv:1710.05463, [Nature551,80(2017)]
- Kasliwal, M. M., et al. 2017, *Science*, 358, 1559
- Kass, R. E., & Raftery, A. E. 1995, *Journal of the American Statistical Association*, 90, 773
- Khan, S., Husa, S., Hannam, M., et al. 2016, *Phys. Rev.*, D93, 044007
- Kiziltan, B., Kottas, A., De Yoreo, M., & Thorsett, S. E. 2013, *Astrophys. J.*, 778, 66
- Kobayashi, S., & Meszaros, P. 2003, *Astrophys. J.*, 589, 861
- Koshut, T. M., Kouveliotou, C., Paciesas, W. S., et al. 1995, *Astrophys. J.*, 452, 145
- Kouveliotou, C., Meegan, C. A., Fishman, G. J., et al. 1993, *Astrophys. J.*, 413, L101
- Kreidberg, L., Bailyn, C. D., Farr, W. M., & Kalogera, V. 2012, *Astrophys. J.*, 757, 36
- Lamb, G. P., & Kobayashi, S. 2017, *Mon. Not. Roy. Astron. Soc.*, 472, 4953
- Lazzati, D. 2005, *Mon. Not. Roy. Astron. Soc.*, 357, 722
- Lazzati, D., Morsony, B. J., & Begelman, M. 2009, *Astrophys. J.*, 700, L47
- Lazzati, D., Perna, R., Morsony, B. J., et al. 2018, *Phys. Rev. Lett.*, 120, 241103
- Lien, A., et al. 2016, *Astrophys. J.*, 829, 7
- MacFadyen, A. I., Woosley, S. E., & Heger, A. 2001, *Astrophys. J.*, 550, 410
- Margalit, B., & Metzger, B. D. 2017, *Astrophys. J.*, 850, L19
- Miller, M. C., & Miller, J. M. 2014, *Phys. Rept.*, 548, 1

- Mooley, K. P., Deller, A. T., Gottlieb, O., et al. 2018, *Nature*, 561, 355
- Most, E. R., Weih, L. R., Rezzolla, L., & Schaffner-Bielich, J. 2018, *Phys. Rev. Lett.*, 120, 261103
- Mösta, P., Ott, C. D., Radice, D., et al. 2015, *Nature*, 528, 376
- Narayan, R., Paczynski, B., & Piran, T. 1992, *Astrophys. J.*, 395, L83
- Nitz, A., Harry, I., Brown, D., et al. 2018, *gwastro/pycbc: PyCBC v1.13.2 Release*, , doi:10.5281/zenodo.1596771
- Nuttall, L. K. 2018, *Philosophical Transactions of the Royal Society of London Series A*, 376, 20170286
- Owen, B. J., & Sathyaprakash, B. S. 1999, *Phys. Rev.*, D60, 022002
- Paczynski, B. 1986, *Astrophys. J.*, 308, L43
- Pan, Y., Buonanno, A., Taracchini, A., et al. 2014, *Phys. Rev.*, D89, 084006
- Pannarale, F., & Ohme, F. 2014, *Astrophys. J.*, 791, L7
- Piro, A. L., & Pfahl, E. 2007, *Astrophys. J.*, 658, 1173
- Radice, D., Perego, A., Zappa, F., & Bernuzzi, S. 2018, *Astrophys. J.*, 852, L29
- Romero, G. E., Reynoso, M. M., & Christiansen, H. R. 2010, *Astron. Astrophys.*, 524, A4
- Rossi, E., Lazzati, D., & Rees, M. J. 2002, *Mon. Not. Roy. Astron. Soc.*, 332, 945
- Savchenko, V., et al. 2017, *Astrophys. J.*, 848, L15
- Shibata, M., Karino, S., & Eriguchi, Y. 2003, *Mon. Not. Roy. Astron. Soc.*, 343, 619
- Smartt, S. J., et al. 2017, *Nature*, 551, 75
- Stanek, K. Z., et al. 2003, *Astrophys. J.*, 591, L17
- Sutton, P. J., et al. 2010, *New J. Phys.*, 12, 053034
- Taracchini, A., et al. 2014, *Phys. Rev.*, D89, 061502
- Troja, E., et al. 2017, *Nature*, 551, 71, [Nature551,71(2017)]
- van Putten, M. H. P. M. 2001, *Phys. Rev. Lett.*, arXiv:astro-ph/0107007, [Phys. Rev. Lett.87,091101(2001)]
- van Putten, M. H. P. M., Lee, G. M., Della Valle, M., Amati, L., & Levinson, A. 2014, arXiv:1411.6939, [Mon. Not. Roy. Astron. Soc.444,58(2014)]
- Vedrenne, G., & Atteia, J.-L. 2009, *Gamma-Ray Bursts: The Brightest Explosions in the Universe* (Springer-Verlag Berlin Heidelberg)
- Veitch, J., & Vecchio, A. 2008, *Class. Quant. Grav.*, 25, 184010
- Veitch, J., et al. 2015, *Phys. Rev.*, D91, 042003
- von Kienlin, A., et al. 2014, *Astrophys. J. Suppl.*, 211, 13
- . 2019, arXiv:1901.06158
- Wanderman, D., & Piran, T. 2015, *MNRAS*, 448, 3026
- Wang, X.-Y., & Meszaros, P. 2007, *Astrophys. J.*, 670, 1247
- Was, M., Sutton, P. J., Jones, G., & Leonor, I. 2012, *Phys. Rev.*, D86, 022003
- Williamson, A. R., Biwer, C., Fairhurst, S., et al. 2014, *Phys. Rev.*, D90, 122004
- Woosley, S. E. 1993, *Astrophys. J.*, 405, 273
- Woosley, S. E., & Bloom, J. S. 2006, *Ann. Rev. Astron. Astrophys.*, 44, 507
- Zhang, B. B., et al. 2018, *Nature Commun.*, 9, 447
- Zhang, W., Woosley, S. E., & MacFadyen, A. I. 2003, *Astrophys. J.*, 586, 356
- Özel, F., & Freire, P. 2016, *Ann. Rev. Astron. Astrophys.*, 54, 401
- Özel, F., Psaltis, D., Narayan, R., & McClintock, J. E. 2010, *Astrophys. J.*, 725, 1918